1   **Structural basis for capsid recruitment and coat formation during HSV-1 nuclear egress**

2

3   Elizabeth B. Draganova[1], Jiayan Zhang[2,3,4], Z. Hong Zhou[2,3,4], and Ekaterina E. Heldwein[1,#]

4

5   [1]Department of Molecular Biology and Microbiology, Tufts University School of Medicine,

6   Boston, MA, 02111, USA

7   [2]Department of Microbiology, Immunology & Molecular Genetics, University of California, Los

8   Angeles (UCLA), Los Angeles, California, 90095, USA

9   [3]Molecular Biology Institute, UCLA, Los Angeles, California, 90095, USA

10   [4]California NanoSystems Institute, UCLA, Los Angeles, California, 90095, USA

11

12   [#]Correspondence: Ekaterina Heldwein, Tufts University School of Medicine, 136 Harrison

13   Avenue, Boston, MA 02111; 617-636-0858; katya.heldwein@tufts.edu

14

15   Keywords: HSV-1, herpesvirus, nuclear egress, nuclear egress complex, NEC, membrane

16   budding, capsid budding

17

18 **Abstract**

19   During herpesvirus infection, egress of nascent viral capsids from the nucleus is mediated by the

20   viral nuclear egress complex (NEC). NEC deforms the inner nuclear membrane (INM) around

21   the capsid by forming a hexagonal array. However, how the NEC coat interacts with the capsid

22   and how curved coats are generated to enable budding is yet unclear. Here, by structure-guided

23   truncations, confocal microscopy, and cryoelectron tomography, we show that binding of the

24   capsid protein UL25 promotes the formation of NEC pentagons rather than hexagons. We

25   hypothesize that during nuclear budding, binding of UL25 situated at the pentagonal capsid

26   vertices to the NEC at the INM promotes formation of NEC pentagons that would anchor the

27   NEC coat to the capsid. Incorporation of NEC pentagons at the points of contact with the

28   vertices would also promote assembly of the curved hexagonal NEC coat around the capsid,

29   leading to productive egress of UL25-decorated capsids.

30

31   To replicate, all viruses must assemble their progeny virions and release them from the cell while

32   overcoming many obstacles, including cellular compartmentalization. Viruses are thus experts at

33   hijacking, manipulating, and, sometimes, even remodeling cellular architecture during viral

34   morphogenesis and egress. Identifying and understanding the unique aspects of virus-induced

35   cellular remodeling could unveil targets for therapeutic intervention; yet, we are only beginning

36   to understand the mechanisms behind many of these processes.

37   One prominent example of virus-induced remodeling of cellular architecture can be

38   observed during egress of herpesviruses – enveloped, double-stranded DNA viruses that infect a

39   wide range of hosts, from mollusks to humans. All herpesviruses can establish lifelong, latent

40   infections within the host, from which they can periodically reactivate, spreading to uninfected

41   tissues and hosts and causing a number of ailments. When the virus actively replicates during a

42   primary infection or reactivation of a latent infection, the progeny virions are assembled and

43   released from the cell in a process termed egress whereby herpesvirus capsids traverse cellular

44   membranes twice [reviewed in (Johnson and Baines 2011, Bigalke and Heldwein 2016, Roller

45   and Baines 2017)]. First, nuclear capsids bud at the inner nuclear membrane (INM) forming

46   enveloped vesicles that pinch off into the perinuclear space. These perinuclear viral particles fuse

47   with the outer nuclear membrane, which releases the capsids into the cytosol. Cytoplasmic

48   capsids then bud again at vesicles derived from the *trans*-Golgi network and early endosomes

49   [reviewed in (Johnson and Baines 2011)] to form mature, infectious virions that are released

50   from the cell by exocytosis. Whereas many enveloped viruses acquire their lipid envelopes by

51   budding at the cytoplasmic membranes or the plasma membrane, herpesviruses are unusual

52   among vertebrate viruses in their ability to bud at the nuclear envelope (Bigalke and Heldwein

53   2016).

54   Capsid budding at the nuclear envelope requires two conserved herpesviral proteins, which

55   are named UL31 and UL34 in herpes simplex virus type 1 (HSV-1), that form the nuclear egress

56   complex (NEC) [reviewed in (Mettenleiter et al. 2013, Bigalke and Heldwein 2016, Bigalke and

57   Heldwein 2017)]. The NEC heterodimer is anchored at the INM through the single C-terminal

58   transmembrane helix of UL34 and faces the nucleoplasm (Shiba et al. 2000). UL31 is a nuclear

59   phosphoprotein that colocalizes with UL34 (Chang and Roizman 1993, Reynolds et al. 2001)

60   and interacts with the capsid during nuclear egress (Trus et al. 2007, Yang and Baines 2011).

61   Both UL31 and UL34 are necessary for efficient nuclear egress, and in the absence of either

62   protein, capsids accumulate in the nucleus and viral replication is reduced by several orders of

63   magnitude (Roller et al. 2000, Fuchs et al. 2002).

64   Previously, we discovered that HSV-1 NEC has an intrinsic ability to deform and bud

65   membranes by demonstrating that purified recombinant NEC vesiculates synthetic lipid bilayers

66   *in vitro* without any additional factors or chemical energy (Bigalke et al. 2014). Similar findings

67   were reported with the NEC homolog from a closely related pseudorabies virus (PRV) (Lorenz et

68   al. 2015). Using cryogenic electron microscopy and tomography (cryoEM/ET), we showed that

69   the NEC forms hexagonal "honeycomb" coats on the inner surface of budded vesicles formed *in*

70   *vitro* (Bigalke et al. 2014). Very similar hexagonal coats were observed in capsidless perinuclear

71   vesicles formed *in vivo*, in uninfected cells expressing PRV NEC (Hagen et al. 2015).

72   Additionally, HSV-1 NEC formed a hexagonal lattice of the same dimensions in crystals

73   (Bigalke and Heldwein 2015). The high-resolution crystal structure of the hexagonal NEC lattice

74   revealed interactions at the lattice interfaces (Bigalke and Heldwein 2015), and subsequent work

75   confirmed that mutations that disrupt oligomeric interfaces reduce budding *in vitro* (Bigalke et

76   al. 2014, Bigalke and Heldwein 2015) and *in vivo* (Roller et al. 2010, Arii et al. 2019).

4

77 Collectively, these findings established the NEC as a viral budding machine that generates

78 negative membrane curvature by oligomerizing into a hexagonal coat on the surface of the

79 membrane.

80   What remains unclear, however, is how the NEC achieves appropriate coat geometry

81 compatible with negative membrane curvature formation during budding. A purely hexagonal

82 arrangement is flat, so curvature is typically achieved either by insertions of pentagons as found

83 at 12 vertices of an icosahedron (Zandi et al. 2004), or by inclusion of irregular defects as

84 observed in several viral coats (Heuser 2005, Briggs et al. 2009, Hyun et al. 2011, Schur et al.

85 2015). It is tempting to speculate that the capsid geometry may influence the geometry of the

86 NEC coat. In perinuclear viral particles visualized in infected cells, the NEC coats appear to be

87 tightly associated with the capsid (Hagen et al. 2015). Capsid interactions with the NEC during

88 nuclear budding may be mediated by binding of the capsid protein UL25 to UL31 (Yang and

89 Baines 2011, Yang et al. 2014). Moreover, UL25 forms pentagonal complexes at the vertices of

90 the icosahedral herpesvirus capsids (Furlong 1978, Dai and Zhou 2018). However, it is unknown

91 whether interaction with a mature capsid could promote pentagonal formation within NEC coats

92 and if so, how the NEC coat would be arranged around the capsid.

93   A fortuitous observation that HSV-1 UL25, a capsid protein that decorates the vertices, co-

94 localizes with synthetic liposomes *in vitro* in the presence of the NEC prompted us to investigate

95 interactions between UL25 and NEC and the effect of UL25 on NEC-mediated budding *in vitro*.

96 Here, by confocal microscopy, we show that free UL25 (i.e., not on capsid vertices) inhibits

97 NEC-mediated budding *in vitro*. 3D visualization of the molecular architecture by cryoET

98 further reveals that free UL25 forms a net of interconnected five-pointed stars on top of

99 membrane-bound NEC layer that may block budding by preventing membrane-bound NEC coats

5

100   from undergoing conformational changes required for budding. We also found that the NEC

101   forms an alternative pentagonal, rather than hexagonal, arrangement when bound to the UL25,

102   and that this phenomenon requires residues 45-73 that form the UL25/UL25 helical bundles on

103   the native capsids. We hypothesize that during nuclear budding, NEC pentagons formed at the

104   points of contact with the capsid vertices both help anchor the NEC coat to the capsid and

105   generate appropriate coat curvature through the inclusion of pentagons into a hexagonal coat as it

106   assembles around the capsid. This mechanism would ensure successful budding and egress of the

107   UL25-decorated viral capsid.

108

109   **RESULTS**

110   *Generation of UL25 variants.* HSV-1 UL25 can be expressed in soluble form in *E. coli* only

111   when residues 1-44 are deleted (Bowman et al. 2006). Residues 1-50 are necessary and sufficient

112   for capsid binding (Cockrell et al. 2009), and in the cryoEM structure of the HSV-1 capsid, these

113   residues mediate extensive interactions with another capsid protein, UL17 (Dai and Zhou 2018).

114   This suggests that these residues are likely disordered in free UL25, potentially leading to

115   aggregation and poor solubility. Therefore, we generated and expressed an HSV-1 UL25Δ44

116   construct, which lacks residues 1-44. UL25Δ44 was soluble and could be purified, in agreement

117   with the previous report (Bowman et al. 2006), but was proteolytically cleaved during

118   purification despite the presence of protease inhibitors (Fig. 1b). N-terminal sequencing (data not

119   shown) of the cleavage product revealed that UL25Δ44 was cut between residues Q72 and A73.

120   To prevent heterogeneity due to cleavage, we generated two constructs: UL25Δ44 Q72A, which

121   has a single point mutation that should eliminate the cleavage site, and UL25Δ73, which

6

122   corresponds to the cleavage product. Both constructs yielded a single UL25 species after

123   purification (Fig. 1b).

124

125   ***UL25Δ44 Q72A inhibits NEC-mediated budding.*** To assess the effect of UL25 on NEC-

126   mediated budding, we used an established *in-vitro* budding assay utilizing recombinant, soluble

127   NEC220 (full-length UL31 and UL34 residues 1-220), fluorescently labelled giant unilamellar

128   vesicles (GUVs), and membrane-impermeable fluorescent dye, Cascade Blue (Bigalke et al.

129   2014). NEC220 and UL25Δ44 Q72A were added to the GUVs in 1:1, 1:6, 1:8, 1:10, or 1:20

130   molar ratios, and budding events were quantified. UL25Δ44 Q72A inhibited NEC-mediated

131   budding in a dose-dependent manner, and at 1:10 or 1:20 NEC:UL25 molar ratios, few budding

132   events were observed (Fig. 1c). By contrast, UL25Δ73 did not inhibit budding even at a 1:20

133   ratio of NEC:UL25 (Fig. 1c), which suggested that residues 45-73 were necessary for inhibition.

134   UL25Δ44 consists of a long N-terminal α-helix (residues 48-94), followed by a flexible

135   linker unresolved in the cryoEM structure, and a C-terminal globular core (residues 134-580)

136   (Fig. 1a). Residues 45-73 encompass the N-terminal half of the long α-helix. To further narrow

137   down the inhibitory region within UL25, we analyzed its sequence conservation. Sequence

138   alignment of UL25 homologs from five alphaherpesviruses revealed a divergent N terminus

139   followed by a highly conserved alanine-rich region, residues 61-69 (Fig. 1a). We generated the

140   UL25Δ58 Q72A construct lacking the divergent N terminus of the α-helix (Fig. 1b). UL25Δ58

141   Q72A did not inhibit NEC220 budding (Fig. 1c). We also generated a UL25Δ50 Q72A construct

142   (as a control for studies using eGFP-UL25 chimera described below), which inhibited budding at

143   a 1:10 NEC:UL25 ratio, the minimal UL25 concentration for budding inhibition (Fig. 2a). Thus,

144   residues 51-73 appear essential for inhibition whereas residues 45-50 are dispensable.

7

145
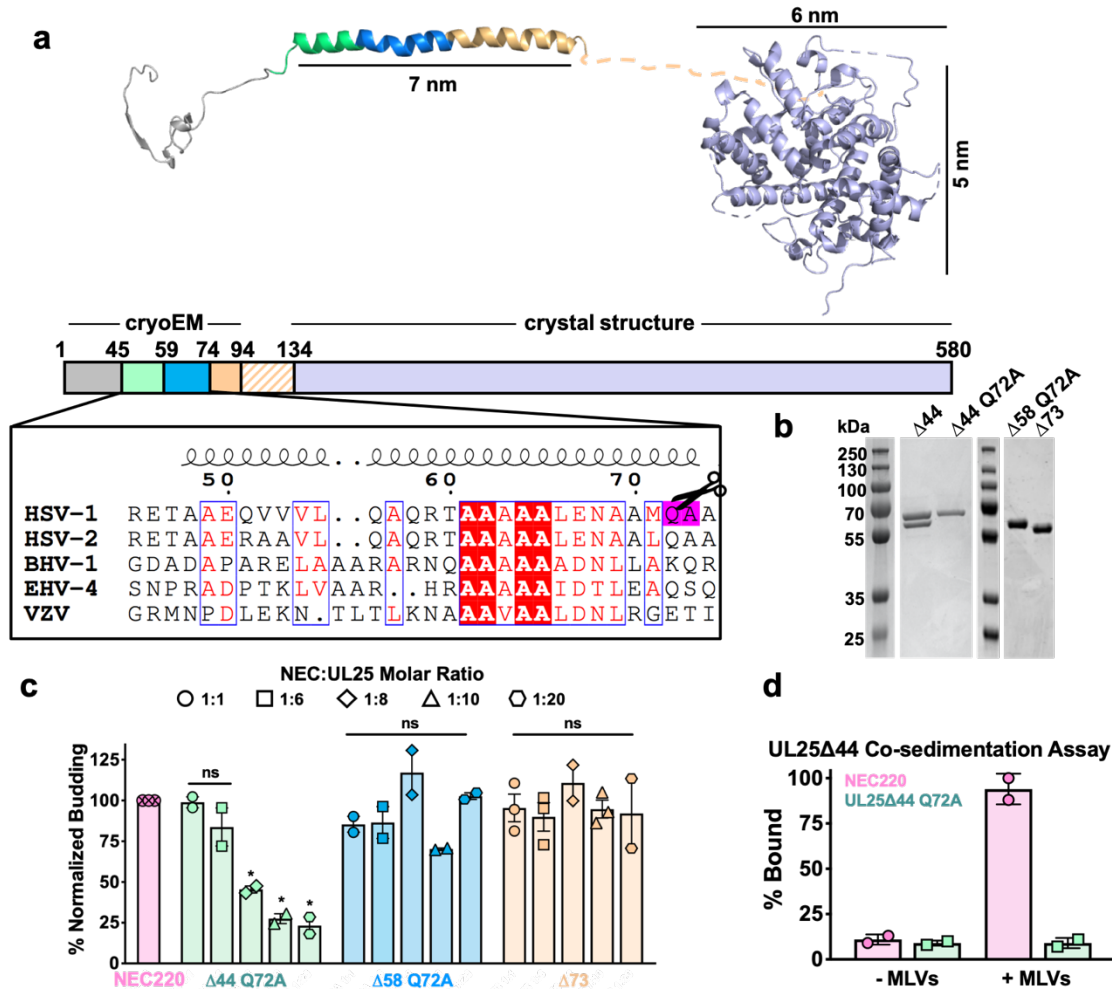
Fig. 1. Inhibition of NEC-mediated budding by UL25 constructs. a) The UL25 structure and a diagram of domain organization is shown along with a multiple sequence alignment of UL25 residues 45-74 from five alphaherpesviruses. Sequence alignment was generated using Clustal Omega[45] and displayed using ESPript 3.0[46]. Identical residues are shown as white letters on a red background. Similar residues are shown as red letters in a blue box. Secondary structure derived from the cryoEM reconstruction of HSV-1 UL25 is shown above the alignment. The following herpesvirus sequences were used (GenBank GeneID numbers in parentheses): HSV-1, herpes simplex virus type 1, strain 17 (2703377); HSV-2, herpes simplex virus type 2, strain HG52 (1487309); BHV-1, bovine herpesvirus-1 (4783418); EHV-4, equine herpesvirus-4, strain NS80567 (1487602); and VZV, varicella-zoster virus, strain Dumas (1487687). **b)** SDS-PAGE of purified UL25 constructs: UL25Δ44 (cleaved product; 57 kDa), UL25Δ44 Q72A (single product; 57 kDa), UL25Δ58 Q72A (56 kDa) and UL25Δ73 (54 kDa). **c)** UL25Δ44 Q72A inhibits NEC budding whereas other UL25 constructs do not. For each condition, NEC-mediated budding was tested at 1:1, 1:6, 1:8, 1:10, and 1:20 NEC:UL25 molar ratios. Each construct was tested in at least two biological replicates, consisting of three technical replicates. Symbols show average budding efficiency of each biological replicate relative to NEC220 (100%; pink). Error bars represent the standard error of measurement for at least two individual experiments. Significance compared to NEC220 was calculated using an unpaired t-test against NEC220. *P-value < 0.1. **d)** UL25Δ44 Q72A does not bind to acidic lipid membranes.

8

164 ***UL25 does not bind synthetic membranes.*** We first tested whether UL25 inhibited NEC-

165 mediated budding by competing with the NEC for binding to membranes. We utilized an

166 established co-sedimentation assay utilizing multilamellar vesicles (MLVs) of the same

167 composition as the GUVs used in the budding assay (Bigalke et al. 2014). Unlike NEC220,

168 UL25Δ44 Q72A did not bind synthetic lipid vesicles (Fig. 1d) and, therefore, could not compete

169 with the NEC220 for binding to membranes.

170

171 ***UL25Δ44 and NEC do not interact in solution.*** UL25 does not bind membranes (Fig. 1d) so, to

172 inhibit NEC-mediated budding, UL25 must instead bind to the NEC. However, no binding was

173 detected in solution, either between UL25Δ44 and NEC220 by isothermal titration calorimetry

174 (Supplementary Fig. S1) or between UL25Δ44 and NEC185Δ50 [a truncated construct that was

175 crystallized previously (Bigalke and Heldwein 2015)] by size-exclusion chromatography

176 (Supplementary Fig. S1). Therefore, to bind UL25, NEC may need to be bound to the membrane.

177 Surface plasmon resonance experiments were also performed, but significant nonspecific binding

178 precluded clear data interpretation (data not shown).

179

180 ***Both inhibitory UL25Δ44 Q72A and non-inhibitory UL25Δ73 colocalize with membranes in***

181 ***the presence of the NEC.*** To visualize UL25 localization in the presence of NEC and

182 membranes by confocal microscopy, we generated the eGFP-tagged versions of the inhibitory

183 and non-inhibitory UL25 constructs, eGFP-UL25Δ44 Q72A and eGFP-UL25Δ73. However,

184 eGFP-UL25Δ44 Q72A construct was unstable during purification, so eGFP-UL25Δ50 Q72A

185 was generated instead. eGFP-UL25Δ50 Q72A (as well as its untagged version UL25Δ50 Q72A)

186 efficiently inhibited NEC-mediated budding whereas eGFP-UL25Δ73 did not (Fig. 2a). When

9

187   eGFP-tagged UL25 constructs were incubated with the fluorescently labelled GUVs, no eGFP

188   signal was detected on the GUV membranes (data not shown), confirming that UL25 did not

189   bind membranes directly.
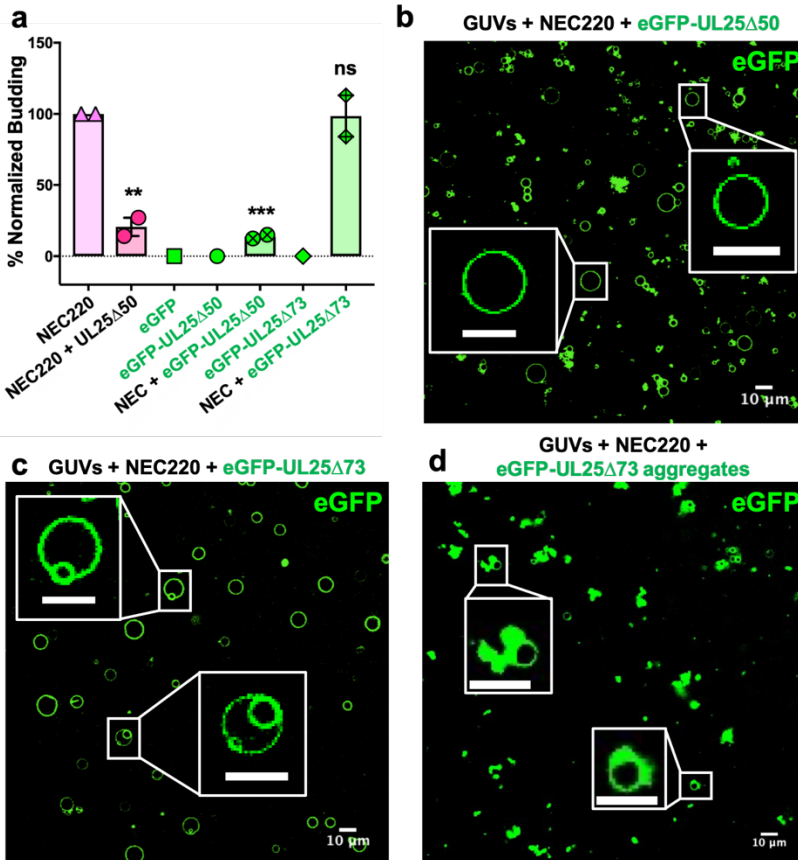
190

191   **Fig. 2. eGFP-UL25Δ50 inhibits NEC budding while eGFP-UL25Δ73 does not. a)** Quantification of
192   NEC budding in the presence of either eGFP-UL25Δ50 or eGFP-UL25Δ73. Each construct (except in the
193   absence of NEC220) was tested in at least two biological replicates, each consisting of three technical
194   replicates. Symbols show the average budding efficiency of each biological replicate relative to NEC220
195   (100%). Error bars represent the standard error of measurement for at least two individual experiments.
196   Significance compared to NEC220 was calculated using an unpaired t-test against NEC220. **P-value <
197   0.01 and ***P-value < 0.001. **b)** Confocal image of eGFP-UL25Δ50 bound to NEC-coated vesicles. No
198   budding is observed. **c)** Confocal image of eGFP-UL25Δ73 either bound to or budded into vesicles with
199   the NEC. **d)** Confocal image of eGFP-UL25Δ73 aggregating on the surface of NEC-coated vesicles. All
200   scale bars = 10 μm.

201   Next, eGFP-UL25Δ50 was incubated with the GUVs in the presence of the NEC220, at a

202   1:10 molar ratio of NEC to UL25 (the minimal inhibitory UL25 concentration). In the presence

203   of the NEC220, the eGFP-UL25Δ50 colocalized with the GUV membranes, and very little

10

204   budding was detected (Fig. 2b). UL25 itself does not bind membranes, so instead it must be

205   binding NEC that is bound to the surface of the GUVs.

206   In the presence of the NEC220, eGFP-UL25Δ73 also colocalized with the GUV

207   membranes. In this case, the eGFP signal was sometimes detected on the membranes of

208   intraluminal vesicles (ILVs) inside the GUVs (Fig. 2c) – a product of budding – which

209   confirmed that binding of eGFP-UL25Δ73 to the NEC220 did not interfere with budding (Fig.

210   2a) and that eGFP-UL25Δ73 could even remain bound to the NEC-coated membranes

211   throughout budding.

212   In many cases, however, the eGFP-UL25Δ73 was clustered around the unbudded GUVs,

213   probably due to its aggregation (Fig. 2d). Such aggregation was not observed for eGFP-

214   UL25Δ50 Q72A (Fig. 2b). It is conceivable that the absence of half of the long N-terminal helix

215   of UL25 (Fig. 1a) leads to aggregation of eGFP-UL25Δ73 on NEC-coated GUVs. Although such

216   aggregation inhibits budding locally (Fig. 2d), bulk measurements show that NEC-mediated

217   budding remains efficient in the presence of eGFP-UL25Δ73 (Fig. 2a). We hypothesize that

218   sequestration of large amounts of aggregated eGFP-UL25Δ73 on a few NEC-coated GUVs

219   reduces its concentration throughout the sample, allowing budding to proceed. Taken together,

220   these results suggested that while both inhibitory and non-inhibitory UL25 constructs could bind

221   the membrane-bound NEC, the binding of the inhibitory UL25 construct blocked NEC-mediated

222   budding whereas the binding of the non-inhibitory UL25 construct did not interfere with it.

223

224   ***Mutations within the putative capsid-binding site on the NEC obviate UL25 inhibition.***

225   Residues D275, K279, and D282 at the membrane-distal tip of UL31 have been implicated in

226   capsid binding in PRV (Ronfeldt et al. 2017) and in HSV-1 (Takeshima et al. 2019). We

11

227   generated a quadruple UL31 mutant in which D275, K279, D282, and a nearby C278 were

228   replaced with alanines. The corresponding mutant NEC220, termed capsid-binding mutant

229   (NEC220-CBM), mediated budding at levels similar to the WT NEC220 (Fig. 3a) but was

230   insensitive to inhibition by UL25Δ44 Q72A (Fig. 3a). Moreover, eGFP-UL25Δ50 Q72A did not

231   co-localize with the GUV membranes in the presence of the NEC220-CBM (Fig. 3b). These

232   results suggested that UL25Δ44 Q72A bound to the membrane-distal tip of UL31 and that this

233   interaction was essential for its inhibitory activity.

234
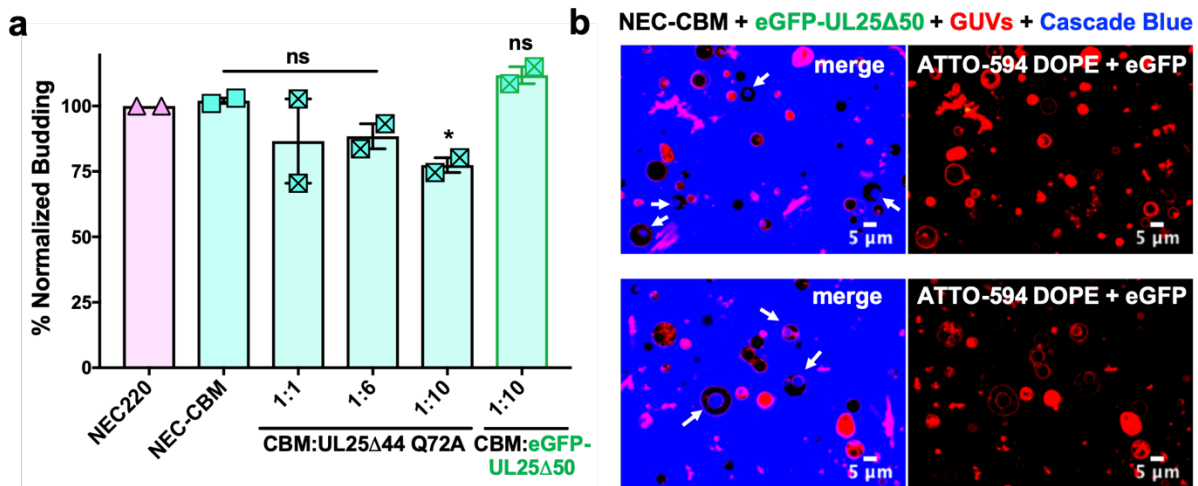
Fig. 3. UL25 does not inhibit NEC-CBM budding. a) NEC-CBM budding is not inhibited by either
UL25Δ44 Q72A or eGFP-UL25Δ50 Q72A. Budding was tested at 1:1, 1:6 and 1:10 NEC220-CBM:UL25
molar ratios for UL25Δ44 Q72A and at a 1:10 NEC-CBM:UL25 molar ratio for eGFP-UL25Δ50 Q72A.
Each condition was tested in at least two biological replicates, each consisting of three technical
replicates. Symbols represent average budding efficiency of each biological replicate relative to NEC220
(100%). Error bars represent the standard error of measurement for at least two individual experiments.
Significance compared to NEC220 was calculated using an unpaired t-test against NEC220. *P-value <
0.1. **b)** Confocal microscopy images showing eGFP-UL25Δ50 Q72A does not bind to NEC-CBM coated
GUVs. Intraluminal vesicles due to NEC-CBM budding are indicated by white arrows. Left column is
merged with the red (ATTO-594 DOPE), green (eGFP), and blue channels (Cascade Blue). Right column
is red (ATTO-594 DOPE) and green (eGFP) only.

246

UL25 binds membrane-bound NEC. To understand how UL25 inhibits NEC-mediated budding,

248   we turned to cryoEM. Previously, we showed that NEC-mediated budding of synthetic large

249   unilamellar vesicles (LUVs) resulted in the formation of smaller vesicles containing ~11-nm

250 thick internal NEC coats (Bigalke et al. 2014). Here, UL25Δ44 Q72A and NEC220 (at a 1:10

251 molar ratio of NEC to UL25) were incubated with LUVs of the same composition as the GUVs

252 used in the budding assay and visualized by cryoEM. In the presence of UL25Δ44 Q72A and

253 NEC220, the LUVs were mostly spherical, and their external surface was coated with ~17-nm

254 thick coats (Fig. 4a) although these typically did not cover the entire surface (Fig. 4a and

255 Supplementary Fig. S2). The external coats formed in the presence of UL25Δ44 Q72A are ~6-

256 nm thicker than the internal NEC coats, and the diameter of the globular portion of UL25 is also

257 ~ 6 nm. Therefore, we hypothesize that the external coats are composed of a UL25Δ44 Q72A

258 layer positioned on top of the membrane-bound NEC220 layer (Fig. 4a). Very few budded

259 vesicles were observed under these conditions, which is consistent with the inefficient budding

260 observed by confocal microscopy (Fig. 1c). Thus, binding of UL25Δ44 Q72A to the NEC220 on

261 the surface of the lipid vesicles correlated with its ability to inhibit NEC-mediated budding.

262
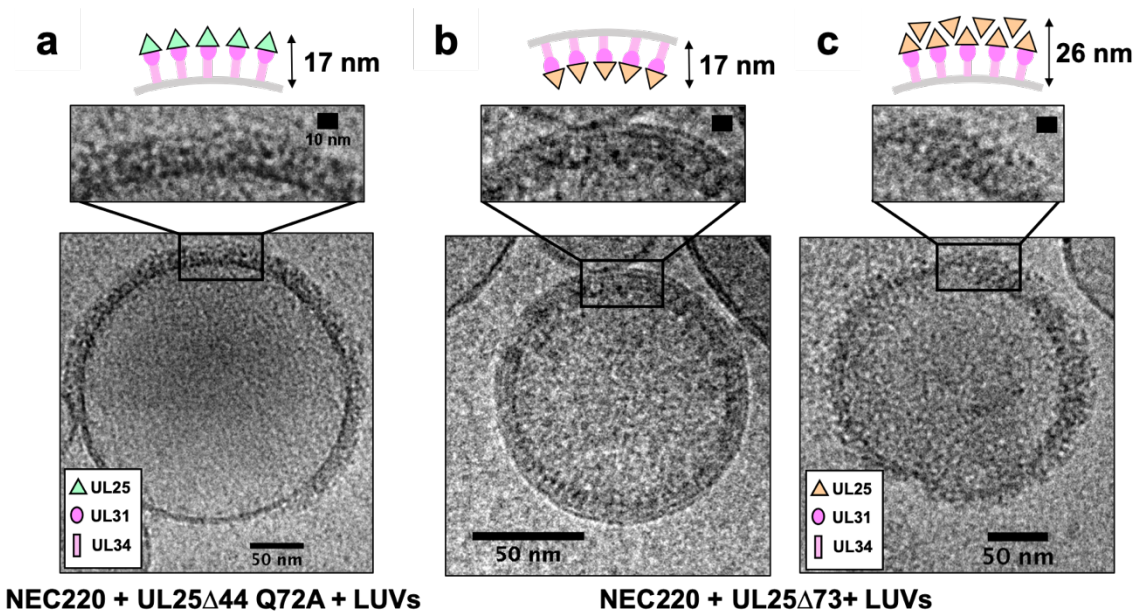
Fig. 4. CryoEM shows UL25Δ44 Q72A inhibits NEC budding while UL25Δ73 does not. CryoEM
images of NEC-mediated budding in the presence of either UL25Δ44 Q72A **(a)** or UL25Δ73 **(b and c)**.
Aggregation of UL25Δ73 is shown in panel C. Scale bars = 50 nm. Inset scale bars = 10 nm.

13

266   Co-incubation of UL25Δ73 and NEC220 with LUVs yielded budded vesicles (Fig. 4b)

267   some of which contained ~17-nm thick internal coats (Fig. 4b), presumably containing UL25Δ73

268   bound to the NEC220, whereas others contained ~11-nm thick internal coats (data not shown),

269   presumably containing only NEC220 (Bigalke et al. 2014). We also observed unbudded LUVs

270   containing >25-nm thick heterogeneous protein aggregates on the external surface (Fig. 4c),

271   similar to UL25Δ73 aggregates observed by confocal microscopy (Fig. 2d).

272

273   ***UL25Δ44 Q72A forms a net of stars bound to NEC pentagons.*** Interactions between UL25Δ44

274   Q72A and membrane-bound NEC220 were visualized in three dimensions by cryoET (Fig. 5).

275   Sub-tomographic averaging of the 3D reconstructions of unbudded LUVs coated with NEC220

276   and UL25Δ44 Q72A (Fig. 5a) revealed that UL25Δ44 Q72A formed a net of five-pointed stars

277   (Fig. 5c) covering the surface of membrane-bound NEC220 whereas the NEC220 formed

278   pentagons (Fig. 5d). Five-pointed stars of UL25 were positioned directly on top of the NEC

279   pentagons (Figs. 5c, d). The star net of UL25 appears to "lock" the NEC layer in place, which

280   could prevent it from undergoing conformational rearrangements required for membrane

281   deformation and budding.

282   The NEC forms hexagonal coats on budded vesicles formed *in-vitro* (Fig. 5b) (Bigalke et

283   al. 2014) and on perinuclear vesicles formed *in vivo* in NEC-expressing uninfected cells (Hagen

284   et al. 2015), so ability of the NEC to form pentagons was unexpected. The NEC pentagons and

285   hexagons have similar dimensions, ~10.5 nm vs. ~11 nm in width (Fig. 5b,d) with ~6.5 nm vs.

286   ~6.3 nm sides (Fig. 5d) (Bigalke et al. 2014). We know that the hexagons are hexamers of the

287   NEC heterodimers (Bigalke and Heldwein 2015). Therefore, we hypothesize that the pentagons

288   are pentamers of the NEC heterodimers. The NEC heterodimers within the pentagons appear

14

289   slightly tilted relative to the plane of the membrane (Fig. 5a) whereas the hexagons are

290   perpendicular to the membrane (Fig. 5b).

291
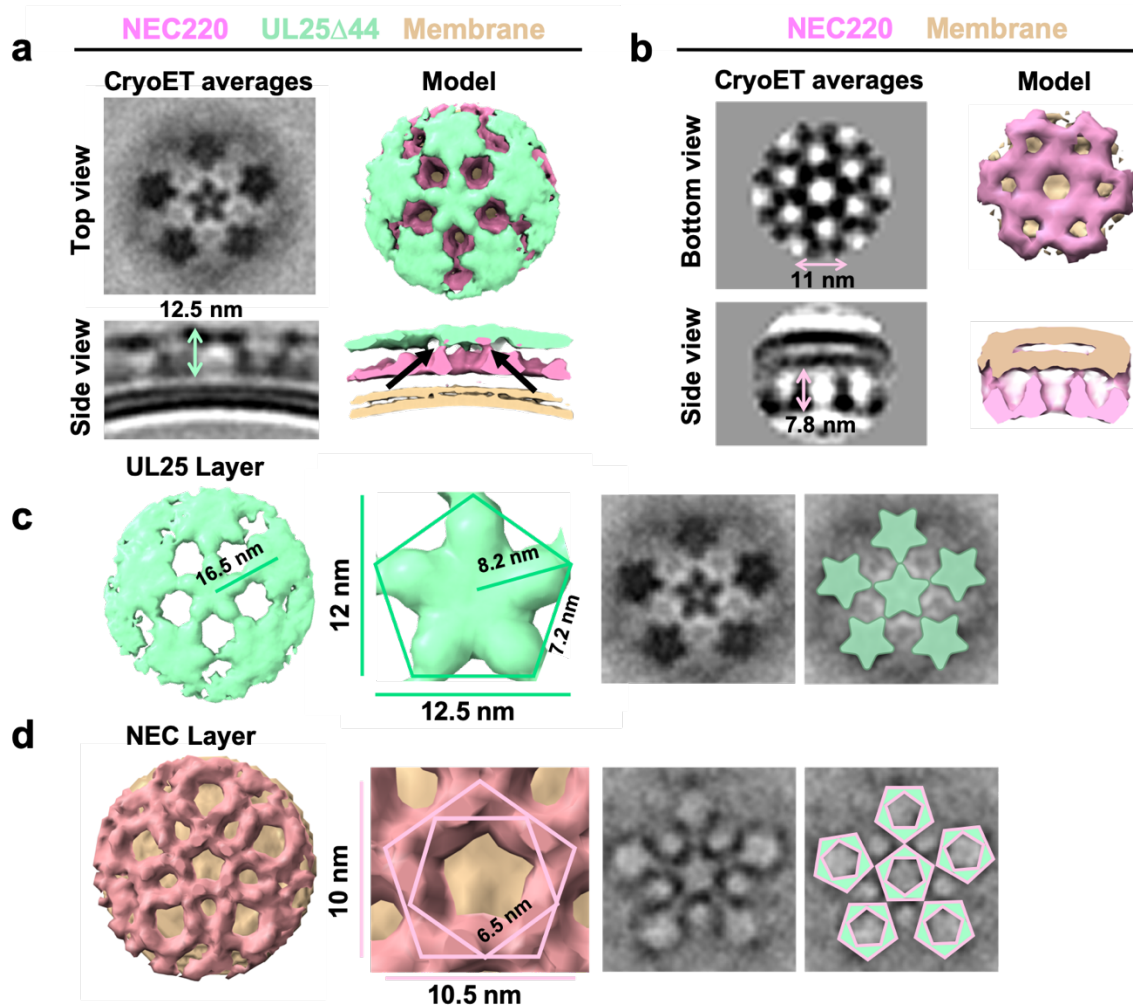
Fig. 5. CryoET of UL25-mediated inhibition of NEC budding. a) CryoET averages of NEC in the presence of UL25Δ44 Q72A (top and side views). Corresponding 3D models are shown with NEC (pink) and UL25Δ44 Q72A (green). The vesicle bilayer is shown in beige. The models show the UL25 layer coating the NEC layer in five-pointed stars on the outside of the vesicles. The length of the NEC-UL25 spikes is 12.5 nm. Black arrows indicate the point of tilt within the NEC layer. **b)** CryoET averages of NEC forming hexameric lattices in the presence of membranes (bottom and side views). Corresponding 3D models are shown with NEC (pink) and the vesicle bilayer (beige). The diameter of the hexameric rings is ~11 nm, while the length of the spikes is 7.8 nm. **c)** CryoET model and averages of the UL25 layer (green) highlighting the five-pointed star formation of UL25 (represented here as a pentamer of dimers) in the presence of NEC. **d)** CryoET model and averages of the NEC layer showing NEC forms a pentagonal lattice (pink pentagons), rather than hexagonal (as seen for wild-type in panel b). Green triangles indicate location of UL25 binding to the NEC.

15

304   It should be noted that an entirely pentagonal lattice would yield a small spherical object

305   with high curvature and icosahedral symmetry – neither of which were observed in our cryoET

306   averages. Given that the NEC/UL25 spikes did not fully coat the vesicles (Fig. 4a), this only

307   permitted averaging of local, rather than global, symmetry, providing a snapshot of NEC/UL25

308   interactions. Furthermore, a mix of both 400 and 800 nm vesicles were used for these

309   experiments, yielding NEC/UL25-bound vesicles of different sizes, resulting in a difference of

310   curvature upon data averaging, ultimately preventing us from mapping the coordinates of each

311   sub-tomogram back onto the raw data to address this issue. Nevertheless, the cryoET data clearly

312   show the ability of the NEC to form an alternative, pentagonal arrangement in the presence of

313   UL25. Our results document the ability of the NEC to form different oligomers.

314

315   **DISCUSSION**

316   The intrinsic ability of the NEC to deform and bud membranes and to oligomerize into a

317   hexagonal coat is well established [reviewed in (Bigalke and Heldwein 2016, Mettenleiter 2016,

318   Bigalke and Heldwein 2017, Roller and Baines 2017)]. However, it is unclear how the capsid

319   triggers the formation of the NEC coat around it or how the NEC coat is anchored to the capsid.

320   Moreover, a purely hexagonal lattice is flat, so it remains unknown how the curvature is

321   generated within the hexagonal NEC coat. Here, we have shown that the NEC forms pentagons

322   when bound to star-shaped UL25 oligomers. We hypothesize that UL25/NEC interactions

323   observed *in vitro* mimic UL25/NEC interactions at the capsid vertices and that NEC pentagons

324   anchor the coat to the capsid. We further hypothesize that NEC pentagons formed at the points of

325   contact with the capsid vertices could nucleate the assembly of and introduce curvature into the

326   hexagonal NEC coats.

16

327 ***UL25 inhibits NEC-mediated budding* in vitro *by forming a star-shaped net over the***

328 ***membrane-bound NEC layer.*** The inhibitory UL25Δ44 Q72A construct, which is composed of a

329 globular core and a long N-terminal helix, formed five-pointed stars linked into a net on the

330 surface of the membrane-bound NEC220 layer. The five-pointed stars formed by UL25 in our

331 cryoET reconstructions resemble the five-pointed stars that crown each capsid vertex and are

332 composed of five copies of the capsid-associated tegument complex (CATC) (Dai and Zhou

333 2018) (Fig. 6a). Each CATC is composed of two copies of UL25, one copy of UL17, and two
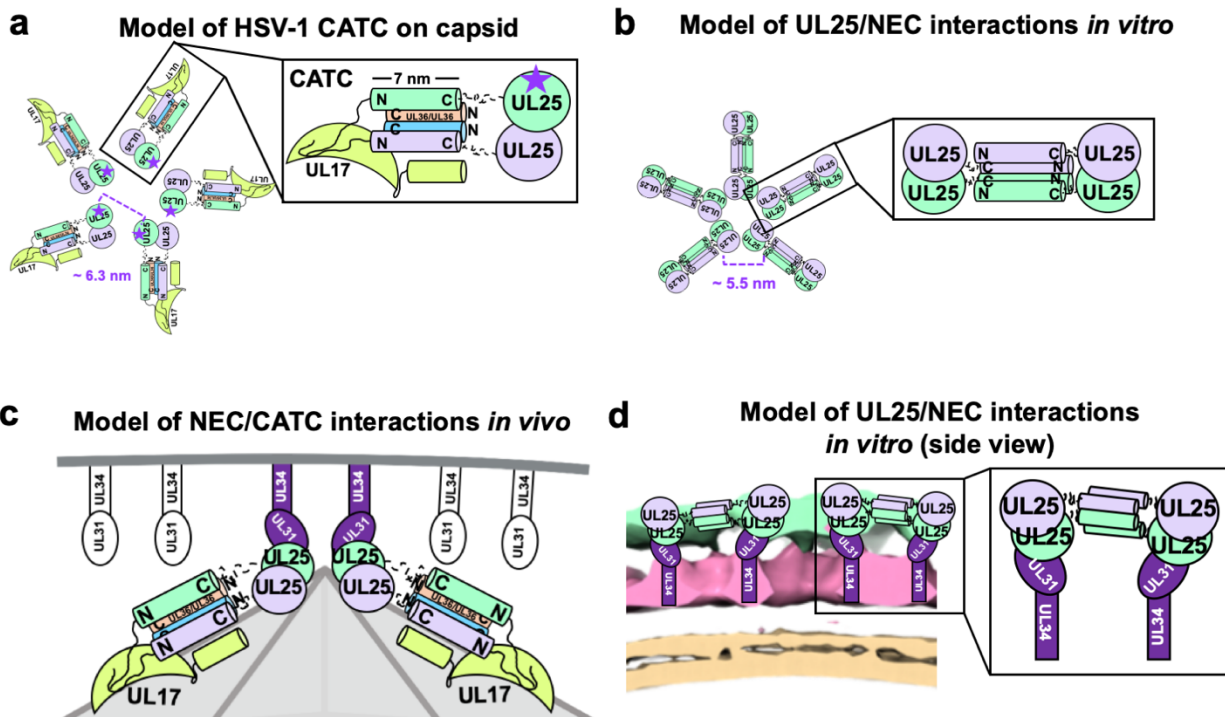
334

335 **Fig. 6. Models of UL25/UL25 and UL25/NEC interactions *in vitro* and *in vivo*.** a) A schematic
336 representation of the pentagonal HSV-1 CATC [two copies of UL25 (green and purple), two copies of C-
337 terminal UL36 (peach and blue) and one copy of UL17 (lime green)] arrangement at the capsid vertex.
338 Inset shows a close-up view of the characteristic antiparallel four-helix bundle composed of two UL25
339 helices and two UL36 helices. Purple stars indicate the proposed UL25 copies that bind to the NEC upon
340 capsid docking. The distance between the centers of two adjacent inner UL25 cores (green) in the capsid
341 (Dai & Zhou, 2018) is ~6.3 nm. b) Proposed model of the UL25 stars formed *in vitro*. The distance
342 between the centers of two adjacent UL25 dimers is ~5.5 nm. Inset shows a close-up view of the proposed
343 antiparallel four-helix bundle composed of two pairs of UL25 helices from adjacent stars. We hypothesize
344 that four-helix bundles link the neighboring UL25 stars into a net. c) Proposed side-view model of the
345 NEC (purple) interacting with the most surface exposed capsid-bound UL25 (green), resulting in a
346 pentameric NEC (indicated by dark purple coloring). NEC molecules prior to capsid binding are shown in
347 an unknown oligomeric state (white). d) Side view of the proposed NEC/UL25 interactions *in vitro*.

17

348 copies of the C-terminal portion of the tegument protein UL36 (Dai and Zhou 2018) and has a

349 characteristic antiparallel four-helix bundle composed of two UL25 helices and two UL36

350 helices (Fig. 6a).

351 We hypothesize that when bound to the NEC220 on the membrane surface *in vitro*,

352 UL25Δ44 Q72A also forms an antiparallel four-helix bundle. Only in this case, the bundle is

353 composed of two pairs of UL25 helices from adjacent stars (Fig. 6b). We hypothesize that four-

354 helix bundles link the neighboring UL25 stars into a net. This arrangement of UL25 would

355 require that each UL25 "star" consist of 10 copies of UL25, with cores arranged in the center and

356 5 pairs of helices radiating out (Fig. 6b). The UL25 cores bind the NEC (Fig. 6d), consistent with

357 previous studies (Yang et al. 2014).

358 Based on our observations, we propose the following model of NEC-mediated budding *in*

359 *vitro* and its inhibition by UL25 (Fig. 7). *In vitro*, the NEC-mediated membrane budding leads to

360 the formation of negative membrane curvature and the internal NEC coats on the budded vesicles

361 (Fig. 7a). UL25Δ44 Q72A binds the membrane-bound NEC and forms five-pointed stars on top

362 of NEC pentagons (Fig. 7b) that are linked into a net. Formation of this net could inhibit budding

363 by restricting conformational changes within the NEC lattice necessary to generate negative

364 membrane curvature. By contrast, UL25Δ73 construct does not inhibit budding. Residues 45-73

365 form about half of the 7-nm-long N-terminal helix (Fig. 1a). Their removal probably precludes

366 formation of stable four-helix bundles. UL25Δ73 is also prone to aggregation likely because the

367 shorter helix is less stable (Fig. 7c).

368

369

370

371
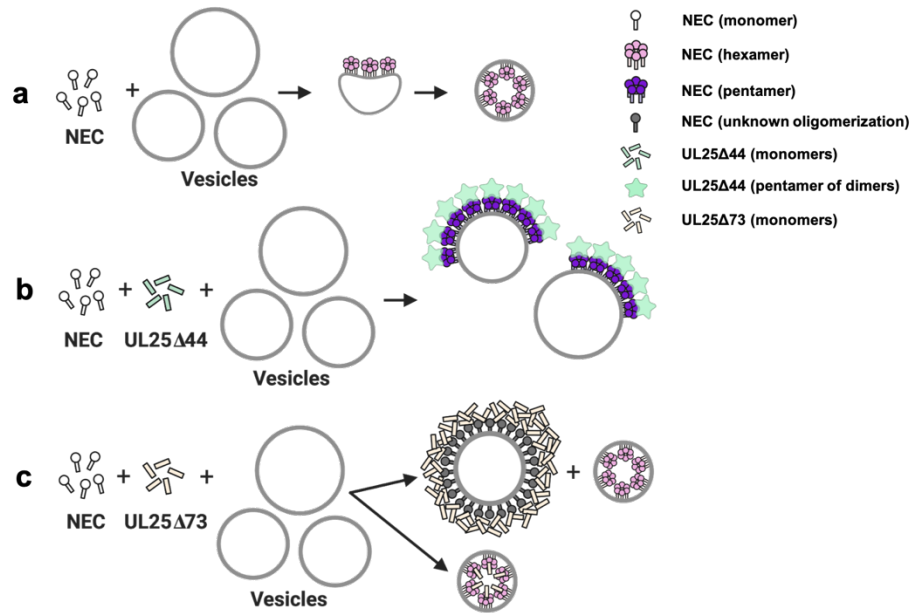
Fig. 6. A model of NEC-mediated budding in the absence and presence of UL25, in vitro. a) NEC-mediated budding requires only the NEC, which vesiculates membranes by forming hexagonal coats (pink) that, potentially, contain irregular defects to achieve curvature. **b)** UL25Δ44 Q72A (green) inhibits NEC-mediated budding by inducing the formation of a pentagonal NEC coat (purple) suboptimal for budding. **c)** UL25Δ73 (peach) aggregates around some NEC-coated vesicles, which blocks budding. Sequestration of UL25Δ73 at a few locations reduces its concentration elsewhere and enables budding. Binding of UL25Δ73 to NEC in the absence of aggregation does not interfere with budding, and bound UL25Δ73 buds into vesicles with the NEC. This figure was created with Biorender.com.

Inhibition of NEC-mediated budding by UL25 is likely an* in-vitro *phenomenon. The robust

budding ability of the NEC, which is observed both *in vitro* or in NEC-expressing uninfected

cells, must be controlled during infection to ensure budding of only mature capsids and to

prevent premature, non-productive budding. NEC budding is presumably negatively regulated by

a viral protein. It is tempting to speculate that UL25 could inhibit the budding activity of the

NEC not only *in vitro* but also during infection. Free UL25 is likely present within the nucleus,

but if it were to inhibit NEC-mediated budding, it would then be expected to bind the accumulate

at the nuclear rim and accumulate there. Yet, such accumulation has not yet been observed.

Therefore, inhibition of NEC-mediated budding by UL25 is likely an *in vitro* phenomenon.

Instead, we hypothesize that interactions between UL25 and membrane-bound NEC, which we

19

390   observed by cryoET and which likely result in budding inhibition *in vitro*, mimic interactions of

391   the NEC with UL25 on the capsid vertices.

392

393   ***UL25/NEC interactions* in vitro *mimic interactions between CATC at the capsid vertices and***

394   ***the NEC coats during infection.*** We observed that when bound to UL25 *in vitro*, the NEC

395   formed pentagons, which established that the NEC can oligomerize into both hexamers and

396   pentamers and that the oligomeric state of the NEC was influenced by UL25. We hypothesize

397   that NEC pentagons formed at the points of contact with the capsid vertices help anchor the NEC

398   coat to the capsid.

399
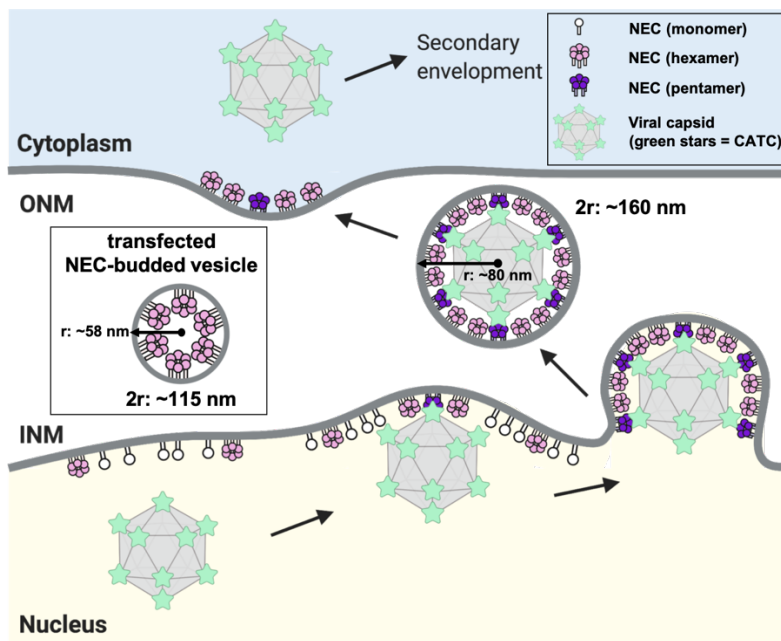
Fig. 7. A model of NEC-mediated budding in HSV-1 infected cells. Capsid-bound UL25 induces the
formation of pentagonal insertions (purple pentamers) within the NEC coat (pink hexamers and white
monomers) as it is forming, which enables the formation of an NEC coat of appropriate size and curvature
around the capsid. Inset shows a transfected NEC-budded vesicle which forms a hexagonal coat with
presumably irregular defects, similar to the NEC coat formed in vitro. This figure was created with
Biorender.com.

406   Each capsid vertex is crowned by a five-pointed star composed of five copies of CATC,

407   with 10 globular cores of UL25 arranged in the center as loosely associated dimers (Fig. 6a) (Dai

20

408   and Zhou 2018). We hypothesize that binding of the cores of five neighboring CATC copies at

409   each capsid vertex (Figs. 6a, b) to the NEC promotes formation of pentagons that attach the coat

410   to the capsid vertices through increased avidity (Fig. 8). The distance between the presumed

411   locations of the cores within the UL25 stars observed *in vitro* is ~5.5 nm (Fig. 6b). The distance

412   between the cores of the innermost UL25 copies within the CATC stars is somewhat longer, ~6.3

413   nm (Fig. 6a), but the cores could move into most favorable orientations for binding the NEC.

414   The dynamic nature of the UL25 cores is evident from the cryoEM reconstructions, which show

415   the cores connected to the N-terminal helices by long, flexible linkers (Dai and Zhou 2018). On

416   the other hand, the NEC may be able to tilt relative to the membrane surface (Fig. 5a), which

417   would also allow each NEC to adopt the optimal orientation for binding the UL25 cores at the

418   capsid vertices.

419   UL25 and the NEC – a monomer and a heterodimer, respectively – do not interact in

420   solution but do interact when the NEC is bound to the membrane, which implies the importance

421   of avidity in binding. The oligomeric state of the NEC prior to the arrival of the capsid is

422   unknown, but high concentration of the NEC at the inner nuclear membrane (Hagen et al. 2015,

423   Newcomb et al. 2017) would provide enough NEC copies locally to form a binding site for

424   UL25 at the capsid vertex.

425   UL25 likely binds to the membrane-distal tip of UL31 because mutations within that

426   region render NEC-CBM mutant insensitive to inhibition by UL25. These results are in

427   agreement with the study by Takeshima *et al.* that showed this UL25-NEC interaction involved

428   UL31 residues R281 and D282 (Takeshima et al. 2019). Other charged residues within the

429   membrane-distal region of UL31 have also been implicated in capsid interactions in PRV

430   (Ronfeldt et al. 2017). Thus, we hypothesize that binding of the capsid to the NEC during

21

431   nuclear egress are mediated by UL25/UL31 interactions. Indeed, NEC185Δ50 (a previously

432   crystallized truncated construct with an intact membrane-distal UL31 region) from *E. coli* binds

433   purified nucleocapsids from HSV-1 infected cells, and this interaction requires UL25 rather than

434   the VP5, VP23, or UL17 capsid proteins (Takeshima et al. 2019). Nucleocapsids can also bind

435   free UL31 (Yang and Baines 2011, Yang et al. 2014).

436

437   ***How does the hexagonal NEC lattice achieve curvature?*** The ability of the NEC to oligomerize

438   into a hexagonal lattice *in vitro* and *in vivo* is well documented (Bigalke et al. 2014, Bigalke and

439   Heldwein 2015, Hagen et al. 2015) and is an important feature of its membrane deformation

440   mechanism (Roller et al. 2010, Bigalke et al. 2014, Bigalke and Heldwein 2015). But how the

441   hexagonal NEC lattice accommodates curvature is yet unclear.

442   A strictly hexagonal lattice is flat, so the curvature is typically achieved through the

443   inclusion of lattice defects, also termed insertions. These can either be regular insertions of a

444   different geometry, for example, pentagons – as observed in icosahedral or fullerene-like capsids

445   – or irregular insertions. Although no deviations from the hexagonal symmetry have yet been

446   visualized in any NEC coats (Bigalke et al. 2014, Hagen et al. 2015, Newcomb et al. 2017), this

447   could be due to the low resolution of the cryoET reconstructions or the imposition of symmetry

448   in averaging. For example, one study used cryoEM and cryoET to visualize NEC/capsid

449   interactions within perinuclear enveloped virions isolated from cells infected with an US3

450   kinase-null HSV-1 (Newcomb et al. 2017), a mutation that causes the accumulation of

451   perinuclear enveloped virions. Although only the hexagonal NEC arrays were observed, the

452   averaging of NEC/CATC interactions was hindered by significant noise in the relevant regions

453   of the tomograms because the NEC coat did not have the same icosahedral symmetry as the

22

454   capsid. As the result, NEC/CATC interactions were difficult to visualize. Additionally, the lack

455   of US3 could have altered the structure of the NEC coat or the NEC/CATC interactions.

456   In perinuclear viral particles formed in PRV-infected cells, the NEC coats appear tightly

457   associated with the capsid (Hagen et al. 2015). Capsidless perinuclear vesicles formed in

458   uninfected cells expressing PRV NEC (Hagen et al. 2015) are relatively uniform in size (~115

459   nm in diameter; Fig. 8, inset) but smaller than the capsid (~125 nm in diameter (Liu et al. 2017,

460   Dai and Zhou 2018)) or the perinuclear vesicles isolated from cells infected with the HSV-1

461   US3-null mutant virus (~160 nm in diameter (Newcomb et al. 2017)) (Fig. 8). The capsid thus

462   appears to define the size of NEC-budded vesicles during infection, so the capsid geometry could

463   influence the geometry of the NEC coat.

464   Based on our observation that the NEC forms pentagons when bound to UL25, we

465   hypothesize that during nuclear egress, NEC pentagons formed at the points of contact with the

466   capsid vertices not only anchor the NEC coat to the capsid but also generate NEC coat of

467   appropriate curvature through the inclusion of pentagons into a hexagonal coat as it assembles

468   around the capsid. A similar strategy is observed during HIV-1 capsid formation by the Gag

469   protein (Briggs et al. 2009, Schur et al. 2015). As the mature capsid is built, the Gag protein is

470   cleaved, and the Gag capsid-domain builds a hexagonal lattice containing 12 pentamers to form a

471   closed fullerene-like structure.

472   We do not yet understand how curved NEC coats are assembled in the absence of capsid.

473   Hexagonal NEC coats formed in *in vitro* or in NEC-expressing cells have a smaller diameter

474   than those formed around the capsid (Fig. 8), so they may achieve coat curvature by other means,

475   for example, by having irregular defects. Incorporation of irregular defects into curved hexagonal

476   lattices have been observed for immature HIV capsids formed by Gag protein (Briggs et al.

23

477   2009, Schur et al. 2015) and in early poxvirus envelopes formed by the D13 protein (Heuser

478   2005, Hyun et al. 2011). NEC could, potentially, use a similar strategy in the absence of a

479   capsids.

480

481   ***A model of NEC-mediated capsid budding during infection.*** Based on our observations, we

482   propose the following model of NEC-mediated capsid budding during nuclear egress in infected

483   cells (Fig. 8). Binding of the cores of five neighboring copies of CATC at the capsid vertices to

484   the NEC at the INM would promote formation of NEC pentagons, which would help anchor the

485   capsid to the INM and could also serve as a nucleation event for the assembly of the NEC coat

486   around the capsid. As the hexagonal NEC coat continues to grow, the incorporation of pentagons

487   into the coat at the points of contact with the vertices would both help attach the NEC coat to the

488   capsid and introduce curvature into the NEC coat (Fig. 8).

489   In both HSV-1 and PRV, removal of UL25 results in an accumulation of capsids at the

490   INM, unable to undergo egress (Klupp et al. 2006, Kuhn et al. 2008). Our results suggest that

491   UL25 both anchors the NEC coat to the capsid and contributes to formation of a curved coat.

492   Additionally, our results could potentially explain why mostly mature, DNA-containing C-

493   capsids undergo budding at the INM (Roizman and Furlong 1974, Klupp et al. 2011). A- and B-

494   capsids have fewer UL25 copies on the capsid surface (Newcomb et al. 2006), and we

495   hypothesize that only C-capsids, which contain UL25 at a full occupancy, can generate

496   pentagonal NEC insertions necessary for the formation of an NEC coat around the capsid. In this

497   manner, NEC/UL25 interactions could provide a quality-control mechanism that would favor

498   budding of mature, DNA-containing C-capsids – which have a full UL25 set – over the immature

499   capsid forms with fewer UL25 copies thereby acting as a checkpoint during nuclear egress.

24

518   **AUTHOR CONTRIBUTIONS**

519   E.B.D. and E.E.H. designed and coordinated the project; E.B.D. performed the experiments

520   (with the exception of the ITC and size-exclusion experiments) under the guidance of E.E.H;

521   E.B.D. and J.Z. collected cryoET data under the guidance of Z.H.Z; J.Z. processed the cryoET

522   data; all authors analyzed the data, interpreted the results and wrote the manuscript.

25

523 **COMPETING INTERESTS**

524 The authors declare no competing interests.

525

526 **DATA AVAILABILITY STATEMENT**

527 The EM datasets generated in this study will be deposited into the Electron Microscopy Data

528 Bank and will be immediately available upon publication.

529   **METHODS**

530   *Cloning.* All primers used in cloning are listed in Supplementary Table S1. Codon-optimized

531   UL25 gene from HSV-1 strain KOS was synthesized by GeneArt. Digested PCR fragments

532   encoding UL25Δ44 were subcloned by restriction digest into the pJP4 plasmid, which contains a

533   His$_6$-SUMO-PreScission tag in frame with the BamHI restriction site of the multiple-cloning site

534   in a pET24b vector, creating the pJB104 plasmid. DNA fragments encoding UL25Δ50 and

535   UL25Δ73 were amplified by PCR from pJB104 (UL25Δ44) and subcloned into pJP4 by

536   restriction digest using BamHI and XhoI, creating the UL25Δ50 (pED13) and UL25Δ73

537   (pJB123) plasmids. Site-directed mutagenesis of pJB104 yielded the UL25Δ44 Q72A mutant

538   plasmid (pED03).

539   DNA encoding the eGFP sequence was PCR amplified out of the eGFP-N2 plasmid

540   (Clontech) and subcloned via single-cut restriction digest into the corresponding UL25 plasmid

541   harboring the cleavable His$_6$-SUMO tag [(either UL25Δ50 (pED13) or UL25Δ73 (pJB123)]

542   creating either the eGFP-UL25Δ50 (pED14) or eGFP-UL25Δ73 (pED05) constructs.

543   Site-directed mutagenesis of pKH90 (UL31 1-306) using a splicing by overlap extension

544   protocol(Heckman and Pease 2007) followed by restriction digest into the pJP4 vector was used

545   to create the UL31 D275A/C278A/K279A/D282A mutant (pJB118) in the capsid binding mutant

546   construct (NEC-CBM).

547

548   *Expression and purification of NEC constructs.* Plasmids encoding HSV-1 UL31 1-306

549   (pKH90) and UL34 1-220 (pJB02) were co-transformed into *Escherichia coli* BL21(DE3)

550   LoBSTr cells (Kerafast) to generate NEC220 (Bigalke et al. 2014). Plasmids encoding HSV-1

551   UL31 1-306 D275A/C278A/K279A/D282A (pJB118) and UL34 1-220 (pJB02) were co-

27

552   transformed into *E. coli* BL21(DE3) LoBSTr cells (Kerafast) to generate NEC-CBM. All

553   constructs were expressed using autoinduction at 37 °C in Terrific Broth (TB) supplemented

554   with 100 μg/mL kanamycin, 100 μg/mL ampicillin, 0.2% lactose and 2 mM MgSO$_4$ for 4 h. The

555   temperature was then reduced to 25 °C for 16 h. Cells were harvested at 5,000 x g for 30 min.

556   NEC proteins were purified as previously described(Bigalke et al. 2014) with slight

557   modifications. The NEC220 and NEC-CBM constructs were passed over 2 x 1 mL HiTrap Talon

558   columns (GE Healthcare), rather than ion exchange as previously described, to remove excess

559   cleaved His$_6$-SUMO before injection onto size-exclusion chromatography (as previously

560   described).

561

562   ***Expression and purification of UL25 constructs.*** Plasmids encoding either HSV-1 UL25 or

563   eGFP-UL25 constructs were transformed into *E. coli* BL21(DE3) LoBSTr cells and expressed

564   using autoinduction at 37 °C in TB supplemented with 100 μg/mL kanamycin, 0.2% lactose, and

565   2 mM MgSO$_4$ for 4 h. The temperature was then reduced to 25 °C for 16 h. Cells were harvested

566   at 5,000 x g for 30 min. All purification steps were performed at 4 °C. UL25 constructs were

567   purified in lysis buffer (50 mM Na HEPES pH 7.5, 500 mM NaCl, 1 mM TCEP, and 10%

568   glycerol). Cells were resuspended in lysis buffer supplemented with Complete protease inhibitor

569   (Roche) and lysed with a microfluidizer (Microfluidics). The cell lysate was clarified by

570   centrifugation at 13,000 x g for 35 min and was passed over Ni-NTA sepharose (GE Healthcare)

571   column. The column was subsequently washed with 20 mM and 40 mM imidazole lysis buffer

572   and bound proteins were eluted with 250 mM imidazole lysis buffer. The His$_6$-SUMO tag was

573   cleaved for 16 h using PreScission Protease produced in-house from a GST-PreScission fusion

574   protein expression plasmid. As a final purification step, UL25 constructs were purified with size-

575   exclusion chromatography using either a Superdex 75 or 200 column (GE Healthcare)

576   equilibrated with gel filtration buffer (20 mM Na HEPES, pH 7.0, 100 mM NaCl, and 1 mM

577   TCEP). The UL25 constructs were purified to homogeneity as assessed by 12% SDS-PAGE and

578   Coomassie staining. Fractions containing UL25 were concentrated up to ~30 mg/mL and stored

579   at -80 °C to prevent degradation observed at 4 °C. Protein concentration was determined by

580   absorbance measurements at 280 nm. The typical yield was 35 mg/L of TB culture.

581

582   ***Co-sedimentation assay.*** Co-sedimentation of UL25Δ44 to acidic multilamellar vesicles (MLVs)

583   was performed as previously described (Bigalke et al. 2014). MLVs were prepared in a 3:1:1

584   ratio of 1-palmitoyl-2-oleoyl-glycero-3-phosphocholine (POPC):1-palmitoyl-2-oleoyl-sn-

585   glycero-3-phospho-L-serine (POPS):1-palmitoyl-2-oleoyl-sn-glycero-3-phosphate (POPA)

586   (Avanti Polar Lipids). Background signal in the absence of liposomes is due to protein

587   aggregation during centrifugation.

588

589   ***In vitro GUV budding assays.*** Giant unilamellar vesicles (GUVs; used for their large size and

590   ease of identification at the microscope) were prepared as previously described (Bigalke et al.

591   2014). For NEC220 only budding quantification, a total of 10 μL of GUVs with a 3:1:1 ratio of

592   POPC:POPS:POPA containing ATTO-594 DOPE (ATTO-TEC GmbH) at a concentration of 0.2

593   μg/μL was mixed with 1 μM NEC220 (final concentration), and 0.2 mg/mL (final concentration)

594   Cascade Blue Hydrazide (ThermoFisher Scientific). For the NEC and UL25 titration

595   experiments, 10 μL of GUVs and either 1, 6, 8, 10 or 20 μM of UL25Δ44 Q72A, UL25Δ58

596   Q72A or UL25Δ73 (final concentration) were incubated with 1 μM of NEC220 (final

597   concentration) along with Cascade Blue. For NEC-CBM and UL25 titration experiments, 10 μL

29

598   of GUVs and either 1, 6, or 10 μM of UL25Δ44 Q72A (final concentration) were incubated with

599   1 μM of NEC-CBM (final concentration) along with Cascade Blue. The total volume of each

600   sample during imaging for all experiments was brought to 100 μL with gel filtration buffer and

601   the reaction was incubated for 5 min at 20 °C. Samples were imaged in a 96-well chambered

602   cover-glass. Images were acquired using a Nikon A1R Confocal Microscope with a 60x oil

603   immersion lens at the Tufts Imaging Facility in the Center for Neuroscience Research at Tufts

604   University School of Medicine. Images of NEC budding in the presence of eGFP-UL25

605   constructs were recorded after incubation of 10 μL of GUVs with 10 μM (final concentration) of

606   either eGFP-UL25Δ50 Q72A or eGFP-UL25Δ73 and 1 μM of NEC220 (final concentration).

607   Quantification was performed by counting vesicles in 15 different frames of the sample (~300

608   vesicles total). Raw data values for all experiments are listed in Supplementary Table S2. Each

609   condition was tested in at least two biological replicates. Prior to analysis, the background was

610   subtracted from the raw values. The reported values represent the average budding activity

611   relative to NEC220 (100%). The standard error of the mean is reported for each measurement.

612   Significance compared to NEC220 was calculated using an unpaired one-tailed *t*-test against

613   NEC220.

614

615   ***Isothermal titration calorimetry (ITC).*** ITC measurements were recorded using a Microcal

616   ITC200 (Malvern Panalytical) at the Center for Macromolecular Interactions at Harvard Medical

617   School. A solution of UL25Δ44 (200 μM) was titrated into a solution of NEC220 (20 μM) in 20

618   mM Na HEPES, pH 7.0, 150 mM NaCl, 1 mM TCEP. Control experiments were performed by

619   injecting UL25Δ44 into buffer. Thermograms were plotted by subtracting heats of the control

620   experiments from the sample experiments. The data were not fit due to no detectable binding.

30

621

622   *Cryoelectron microscopy and tomography.* A volume of 10 μL of a 1:1 mixture of 400-nm and

623   800-nm large unilamellar vesicles (LUVs) made of 3:1:1 POPC:POPS:POPA [prepared as

624   previously described (Bigalke et al. 2014)] were mixed on ice with a 30 μL solution of NEC220

625   and either UL25Δ44 Q72A or UL25Δ73, yielding an NEC:UL25 ratio of 1:10 (NEC

626   concentration was at 1 mg/mL). After 30 min, 3 μL of sample was applied to glow-discharged

627   (30 s) Quantifoil copper grids (R2/2, 200 mesh, Electron Microscopy Sciences), blotted on both

628   sides for 4 s, and vitrified by rapid freezing in liquid ethane (Vitrobot). Grids were stored in

629   liquid nitrogen until loaded into a Tecnai F20 transmission electron microscope (FEI) via a cryo

630   holder (Gatan). The microscope was operated in low dose mode at 200 keV using SerialEM

631   (Mastronarde 2005) and images were recorded with a 4k x 4k charge coupled device camera

632   (Ultrascan, Gatan) at 29,000-fold magnification (pixel size: 0.632 nm). 2D cryo-EM images were

633   recorded at defocus values of -4 to -8 μm and an electron dose ~15 e/Å^2. Images are displayed

634   using ImageJ (Schindelin et al. 2015).

635   For single-axis cryoET data used to generate 3D EM data, samples were incubated on ice

636   for 30 min, and 0.8 μL of 10 nm colloidal gold coated with protein A (Cell Microscopy Core,

637   University Medical Center Utrecht, Department of Cell Biology) was added to the solution and

638   mixed. The mixture (2.5 μL) was applied to freshly glow-discharged (30 s) Quantifoil R 3.5/1

639   grids (Electron Microscopy Sciences) and manually blotted before being flash-frozen in liquid

640   ethane. Grids were loaded into a FEI Titan Krios electron microscope equipped with a Gatan

641   imaging filter (GIF) and a Gatan K2 summit direct electron detection camera (Roper

642   Technologies, Inc.), operated at 300 kV. The acquisition for automated cryoET tilt series

643   collection was performed using SerialEM (Mastronarde 2005). A tilt series was collected in

644   which the sample was tilted from 0° to +60° degrees and then from 0° to -60°, each in a stepwise

645   fashion with 2° increments. Tilt series were acquired at a magnification of x53,000

646   (corresponding to a calibrated pixel size of 2.6 Å) with a maintained defocus value of -3 to -4

647   μm. The total electron dose was ~100 e/Å^2.

648

649   ***3D reconstruction and subtomographic averaging.*** The detailed steps of the 3D reconstruction

650   and subtomographic averaging were previously described (Si et al. 2018). Briefly, frames from

651   each recorded tilt series were drift-corrected and averaged with *Motioncorr* (Mastronarde 2005)

652   and was further reconstructed with contrast transfer function (CTF) correction using the IMOD

653   software package (Kremer et al. 1996). Two resulting tomograms were produced by the

654   weighted back projection and simultaneous iterative reconstruction technique (SIRT) methods. A

655   total of 1200 particles were picked for tomograms containing LUVs, NEC220 and UL25Δ44

656   Q72A. 3D sub-tomographic averaging was completed as described(Si et al. 2018) using the

657   PEET (particle estimation for electron tomography) software (Nicastro et al. 2006). Five-fold

658   symmetry was only applied after five-fold symmetry was apparent in the averaged structure. The

659   original dataset was split into two separate groups, even group and odd group, and averaged

660   independently. Gold standard Fourier Shell Correlation (FSC) analysis for the averaged structure

661   was performed by *calcUnbiasedFSC* in PEET when the two averaged structures converged. The

662   reported resolution is 29 Å based on the 0.143 gold-standard FSC criterion. EM maps will be

663   deposited into the Electron Microscopy Data Bank (EMDB) for immediate access upon

664   publication.

665

References

Arii, J., K. Takeshima, Y. Maruzuru, N. Koyanagi, A. Kato and Y. Kawaguchi (2019). "Roles of the Interhexamer Contact Site for Hexagonal Lattice Formation of the Herpes Simplex Virus 1 Nuclear Egress Complex in Viral Primary Envelopment and Replication." Journal of Virology **93**(14).

Bigalke, J. M. and E. E. Heldwein (2015). "Structural basis of membrane budding by the nuclear egress complex of herpesviruses." EMBO Journal **34**(23): 2921-2936.

Bigalke, J. M. and E. E. Heldwein (2016). "Nuclear exodus: Herpesviruses lead the way." Annual Review of Virology **3**(1): 387-409.

Bigalke, J. M. and E. E. Heldwein (2017). "Have NEC coat, will travel: Structural basis of membrane budding during nuclear egress in herpesviruses." Advances in virus research **97**: 107-141.

Bigalke, J. M., T. Heuser, D. Nicastro and E. E. Heldwein (2014). "Membrane deformation and scission by the HSV-1 nuclear egress complex." Nature Communications **5**: 4131.

Bowman, B. R., R. L. Welschhans, H. Jayaram, N. D. Stow, V. G. Preston and F. A. Quiocho (2006). "Structural characterization of the UL25 DNA-packaging protein from herpes simplex virus type 1." Journal of Virology **80**(5): 2309-2317.

Briggs, J. A., J. D. Riches, B. Glass, V. Bartonova, G. Zanetti and H. G. Krausslich (2009). "Structure and assembly of immature HIV." Proceedings of the National Academy of Sciences of the United States of America **106**(27): 11090-11095.

Briggs, J. A., J. D. Riches, B. Glass, V. Bartonova, G. Zanetti and H. G. Krausslich (2009). "Structure and assembly of immature HIV." Proc Natl Acad Sci U S A **106**(27): 11090-11095.

Chang, Y. E. and B. Roizman (1993). "The product of the UL31 gene of herpes simplex virus 1 is a nuclear phosphoprotein which partitions with the nuclear matrix." Journal of Virology **67**(11): 6348-6356.

Cockrell, S. K., M. E. Sanchez, A. Erazo and F. L. Homa (2009). "Role of the UL25 protein in herpes simplex virus DNA encapsidation." J Virol **83**(1): 47-57.

Dai, X. and Z. H. Zhou (2018). "Structure of the herpes simplex virus 1 capsid with associated tegument protein complexes." Science **360**(6384).

Fuchs, W., B. G. Klupp, H. Granzow, N. Osterrieder and T. C. Mettenleiter (2002). "The interacting UL31 and UL34 gene products of pseudorabies virus are involved in egress from the host-cell nucleus and represent components of primary enveloped but not mature virions." Journal of Virology **76**(1): 364-378.

700 Furlong, D. (1978). "Direct evidence for 6-fold symmetry of the herpesvirus hexon capsomere."
701 Proceedings of the National Academy of Sciences of the United States of America **75**(6): 2764-
702 2766.

703 Hagen, C., K. C. Dent, T. Zeev-Ben-Mordehai, M. Grange, J. B. Bosse, C. Whittle, B. G. Klupp,
704 C. A. Siebert, D. Vasishtan, F. J. Bauerlein, J. Cheleski, S. Werner, P. Guttmann, S. Rehbein, K.
705 Henzler, J. Demmerle, B. Adler, U. Koszinowski, L. Schermelleh, G. Schneider, L. W. Enquist,
706 J. M. Plitzko, T. C. Mettenleiter and K. Grunewald (2015). "Structural basis of vesicle formation
707 at the inner nuclear membrane." Cell **163**(7): 1692-1701.

708 Heckman, K. L. and L. R. Pease (2007). "Gene splicing and mutagenesis by PCR-driven overlap
709 extension." Nature Protocols **2**(4): 924-932.

710 Heuser, J. (2005). "Deep-etch EM reveals that the early poxvirus envelope is a single membrane
711 bilayer stabilized by a geodetic "honeycomb" surface coat." Journal of Cell Biology **169**(2): 269-
712 283.

713 Hyun, J. K., C. Accurso, M. Hijnen, P. Schult, A. Pettikiriarachchi, A. K. Mitra and F. Coulibaly
714 (2011). "Membrane remodeling by the double-barrel scaffolding protein of poxvirus." PLoS
715 Pathogens **7**(9): e1002239.

716 Johnson, D. C. and J. D. Baines (2011). "Herpesviruses remodel host membranes for virus
717 egress." Nature Reviews Microbiology **9**(5): 382-394.

718 Klupp, B. G., H. Granzow, G. M. Keil and T. C. Mettenleiter (2006). "The capsid-associated
719 UL25 protein of the alphaherpesvirus pseudorabies virus is nonessential for cleavage and
720 encapsidation of genomic DNA but is required for nuclear egress of capsids." Journal of
721 Virology **80**(13): 6235-6246.

722 Klupp, B. G., H. Granzow and T. C. Mettenleiter (2011). "Nuclear envelope breakdown can
723 substitute for primary envelopment-mediated nuclear egress of herpesviruses." Journal of
724 Virology **85**(16): 8285-8292.

725 Kremer, J. R., D. N. Mastronarde and J. R. McIntosh (1996). "Computer visualization of three-
726 dimensional image data using IMOD." Journal of Structural Biology **116**(1): 71-76.

727 Kuhn, J., T. Leege, B. G. Klupp, H. Granzow, W. Fuchs and T. C. Mettenleiter (2008). "Partial
728 functional complementation of a pseudorabies virus UL25 deletion mutant by herpes simplex
729 virus type 1 pUL25 indicates overlapping functions of alphaherpesvirus pUL25 proteins."
730 Journal of Virology **82**(12): 5725-5734.

731 Liu, Y. T., J. Jiang, K. P. Bohannon, X. Dai, G. W. Gant Luxton, W. H. Hui, G. Q. Bi, G. A.
732 Smith and Z. H. Zhou (2017). "A pUL25 dimer interfaces the pseudorabies virus capsid and
733 tegument." Journal of General Virology **98**(11): 2837-2849.

734 Lorenz, M., B. Vollmer, J. D. Unsay, B. G. Klupp, A. J. Garcia-Saez, T. C. Mettenleiter and W.
735 Antonin (2015). "A single herpesvirus protein can mediate vesicle formation in the nuclear
736 envelope." Journal of Biological Chemistry **290**(11): 6962-6974.

737 Mastronarde, D. N. (2005). "Automated electron microscope tomography using robust prediction
738 of specimen movements." Journal of Structural Biology **152**(1): 36-51.

739 Mettenleiter, T. C. (2016). "Vesicular Nucleo-Cytoplasmic Transport-Herpesviruses as Pioneers
740 in Cell Biology." Viruses **8**(10).

741 Mettenleiter, T. C., F. Muller, H. Granzow and B. G. Klupp (2013). "The way out: what we
742 know and do not know about herpesvirus nuclear egress." Cellular Microbiology **15**(2): 170-178.

743 Newcomb, W. W., J. Fontana, D. C. Winkler, N. Cheng, J. B. Heymann and A. C. Steven
744 (2017). "The primary enveloped virion of herpes simplex virus 1: Its role in nuclear egress."
745 MBio **8**(3).

746 Newcomb, W. W., F. L. Homa and J. C. Brown (2006). "Herpes simplex virus capsid structure:
747 DNA packaging protein UL25 is located on the external surface of the capsid near the vertices."
748 Journal of Virology **80**(13): 6286-6294.

749 Nicastro, D., C. Schwartz, J. Pierson, R. Gaudette, M. E. Porter and J. R. McIntosh (2006). "The
750 molecular architecture of axonemes revealed by cryoelectron tomography." Science **313**(5789):
751 944-948.

752 Reynolds, A. E., B. J. Ryckman, J. D. Baines, Y. Zhou, L. Liang and R. J. Roller (2001).
753 "U(L)31 and U(L)34 proteins of herpes simplex virus type 1 form a complex that accumulates at
754 the nuclear rim and is required for envelopment of nucleocapsids." Journal of Virology **75**(18):
755 8803-8817.

756 Roizman, B. and D. Furlong (1974). The Replication of Herpesviruses. Comprehensive
757 Virology. H. Fraenkel-Conrat and R. R. Wagner. Boston, MA, Springer**:** 229-403.

758 Roller, R. J. and J. D. Baines (2017). "Herpesvirus nuclear egress." Advances in Anatomy,
759 Embryology, and Cell Biology **223**: 143-169.

760 Roller, R. J., S. L. Bjerke, A. C. Haugo and S. Hanson (2010). "Analysis of a charge cluster
761 mutation of herpes simplex virus type 1 UL34 and its extragenic suppressor suggests a novel
762 interaction between pUL34 and pUL31 that is necessary for membrane curvature around
763 capsids." Journal of Virology **84**(8): 3921-3934.

764 Roller, R. J., Y. Zhou, R. Schnetzer, J. Ferguson and D. DeSalvo (2000). "Herpes simplex virus
765 type 1 U(L)34 gene product is required for viral envelopment." Journal of virology **74**(1): 117-
766 129.

767 Ronfeldt, S., B. G. Klupp, K. Franzke and T. C. Mettenleiter (2017). "Lysine 242 within helix 10
768 of the pseudorabies virus nuclear egress complex pUL31 component is critical for primary
769 envelopment of nucleocapsids." Journal of Virology.

770 Schindelin, J., C. T. Rueden, M. C. Hiner and K. W. Eliceiri (2015). "The ImageJ ecosystem: An
771 open platform for biomedical image analysis." Molecular Reproduction and Development **82**(7-
772 8): 518-529.

773 Schur, F. K., W. J. Hagen, M. Rumlova, T. Ruml, B. Muller, H. G. Krausslich and J. A. Briggs
774 (2015). "Structure of the immature HIV-1 capsid in intact virus particles at 8.8 A resolution."
775 Nature **517**(7535): 505-508.

776 Shiba, C., T. Daikoku, F. Goshima, H. Takakuwa, Y. Yamauchi, O. Koiwai and Y. Nishiyama
777 (2000). "The UL34 gene product of herpes simplex virus type 2 is a tail-anchored type II
778 membrane protein that is significant for virus envelopment." Journal of General Virology **81**(Pt
779 10): 2397-2405.

780 Si, Z., J. Zhang, S. Shivakoti, I. Atanasov, C. L. Tao, W. H. Hui, K. Zhou, X. Yu, W. Li, M. Luo,
781 G. Q. Bi and Z. H. Zhou (2018). "Different functional states of fusion protein gB revealed on
782 human cytomegalovirus by cryo electron tomography with Volta phase plate." PLoS Pathog
783 **14**(12): e1007452.

784 Takeshima, K., J. Arii, Y. Maruzuru, N. Koyanagi, A. Kato and Y. Kawaguchi (2019).
785 "Identification of the Capsid Binding Site in the Herpes Simplex Virus 1 Nuclear Egress
786 Complex and Its Role in Viral Primary Envelopment and Replication." Journal of Virology
787 **93**(21).

788 Trus, B. L., W. W. Newcomb, N. Cheng, G. Cardone, L. Marekov, F. L. Homa, J. C. Brown and
789 A. C. Steven (2007). "Allosteric signaling and a nuclear exit strategy: binding of UL25/UL17
790 heterodimers to DNA-Filled HSV-1 capsids." Mol Cell **26**(4): 479-489.

791 Yang, K. and J. D. Baines (2011). "Selection of HSV capsids for envelopment involves
792 interaction between capsid surface components pUL31, pUL17, and pUL25." Proceedings of the
793 National Academy of Sciences of the United States of America **108**(34): 14276-14281.

794 Yang, K., E. Wills, H. Y. Lim, Z. H. Zhou and J. D. Baines (2014). "Association of herpes
795 simplex virus pUL31 with capsid vertices and components of the capsid vertex-specific
796 complex." Journal of Virology **88**(7): 3815-3825.

797 Zandi, R., D. Reguera, R. F. Bruinsma, W. M. Gelbart and J. Rudnick (2004). "Origin of
798 icosahedral symmetry in viruses." Proceedings of the National Academy of Sciences of the
799 United States of America **101**(44): 15556-15560.

800